World Electric Vehicle Journal

MDPI

Article

Performance Optimization of Hydro-Pneumatic Suspension for Mining Dump Trucks Based on the Improved Multi-Objective Particle Swarm Optimization

Lin Yang [1], Tianli Gao [1], Mingsen Zhao [1], Guangjia Wang [1] and Wei Liu [2,*]

[1] School of Automotive and Traffic Engineering, Jiangsu University of Technology, Changzhou 213001, China; yanglin928@jsut.edu.cn (L.Y.); 2024655250@smail.jstu.edu.cn (T.G.); 2024655100@smail.jstu.edu.cn (M.Z.); 2024655242@smail.jstu.edu.cn (G.W.)

[2] School of Automotive and Traffic Engineering, Jiangsu University, Zhenjiang 212013, China

* Correspondence: liuw@ujs.edu.cn

Abstract

Aiming at the challenge of simultaneously optimizing ride comfort and wheel grounding performance for mining dump trucks under severe road conditions, this paper proposes a hydro-pneumatic suspension parameter design method based on an improved multi-objective particle swarm optimization (IMOPSO) algorithm. First, a dynamic model of the hydro-pneumatic suspension is established, incorporating the coupled nonlinear characteristics of the valve system and the gas chamber. The accuracy of the model is verified through bench tests. Subsequently, the influence of key parameters, including the damping orifice diameter, check valve seat hole diameter, and initial gas charging height, on the vertical dynamic performance of the vehicle, is systematically analyzed. On this basis, a multi-objective optimization model is constructed with the objective of minimizing the root mean square (RMS) values of both the sprung mass acceleration and the dynamic tire load. To enhance the global search capability and convergence performance of the MOPSO algorithm, adaptive inertia weighting, dynamic flight parameter update, and an enhanced mutation strategy are introduced. Simulation results demonstrate that the optimized suspension achieves significant improvements under various road conditions. On class-C roads, the RMS values of the sprung mass acceleration (SMA) and the dynamic tire load (DTL) are reduced by 37.6% and 15.8%, respectively, while the suspension rattle space (SRS) decreases by 10.2%. Under transient bump roads, the peak-to-peak (Pk-Pk) values of the same two indicators drop by 38.9% and 44.9%, respectively. Furthermore, compared to the NSGA-II algorithm, the proposed method demonstrates superior performance in terms of convergence stability and overall performance balance. These results indicate that the proposed design effectively balances ride comfort, wheel grounding performance, and driving safety. This study provides a theoretical foundation and an engineering-feasible method for the performance balancing and parameter co-design of suspension systems in heavy-duty engineering vehicles.

Keywords: mining dump truck; hydro-pneumatic suspension; improved multi-objective particle swarm optimization; parameter optimization; performance balancing

Check for updates

Academic Editor: Vladimir Katic

Received: 11 January 2026
Revised: 2 February 2026
Accepted: 3 February 2026
Published: 5 February 2026

Copyright: © 2026 by the authors. Published by MDPI on behalf of the World Electric Vehicle Association. Licensee MDPI, Basel, Switzerland. This article is an open access article distributed under the terms and conditions of the Creative Commons Attribution (CC BY) license.

1. Introduction

As core transport equipment in large-scale open-pit mines, mining dump trucks operate for extended periods under severe working conditions characterized by unstructured

terrain and high-impact roads. Frequent and intense road excitations are transmitted to the vehicle body through the suspension system, significantly threatening ride comfort, handling stability, and the structural reliability of key components [1–5]. Therefore, developing a suspension system capable of effectively absorbing impacts and suppressing vibrations is essential for ensuring the comprehensive performance of the vehicle, enhancing operational efficiency, and improving safety [6–11].

Compared with traditional passive suspension systems, hydro-pneumatic suspension has become an ideal choice for heavy-duty engineering vehicles due to its unique oil–gas composite structure, which combines nonlinear stiffness with adjustable damping, offering excellent vibration isolation and load-bearing performance within limited space [12–14]. The output characteristics of a hydro-pneumatic suspension are determined by its key structural parameters, such as the damping orifice diameter, check valve seat hole diameter, and initial gas pressure. Therefore, coordinating its stiffness and damping properties through parameter optimization represents a key pathway to enhancing vehicle dynamic performance.

In recent years, scholars worldwide have conducted extensive research on the modeling and optimization of hydro-pneumatic suspensions [15–19]. Regarding modeling, efforts have primarily focused on establishing accurate valve system fluid dynamics models and gas polytropic process models to capture their strongly nonlinear force output characteristics [20]. Lv et al. [21] developed a mathematical model for hydro-pneumatic suspension that includes a fractional-order differential term, aiming to describe its nonlinear essence more precisely. By utilizing a modified Oustaloup filter algorithm to perform the fractional-order calculations, the model can reflect the system characteristics with higher accuracy. In addressing the limitation of traditional hydro-pneumatic suspension systems whose damping cannot be adjusted in real time, Jiang et al. [22] introduced a shear-valve magnetorheological hydro-pneumatic spring. They validated this configuration through multiphysics coupling simulations and mechanical tests and further established a nonlinear dynamic model based on the experimental results. In the field of parameter optimization, most research adopts single-objective optimization or experience-based trial-and-error methods, focusing on improving a single performance metric such as ride comfort or wheel grounding performance [23,24]. However, ride comfort and wheel grounding performance are inherently characterized by a trade-off relationship, making it difficult for a single optimization objective to achieve the optimal balance of overall vehicle performance. In contrast, Yang et al. [25] proposed a multi-objective optimization method for hydro-pneumatic hybrid suspensions in articulated dump trucks based on the NLPQL algorithm. They established a comprehensive model integrating vehicle dynamics, steering, and tire systems, effectively coordinating the conflicts among body acceleration, roll angle, and pitch angle. Meanwhile, Kwon et al. [26] introduced a multi-objective optimization approach for hydro-pneumatic hybrid suspensions in heavy-duty vehicles using the NSGA-II algorithm combined with a surrogate model, achieving comprehensive improvements in both ride comfort and roll stability. Although multi-objective optimization algorithms provide an effective framework for addressing such trade-off problems, their application in the coordinated design of hydro-pneumatic suspension parameters remain insufficient. Moreover, existing algorithms often face challenges such as slow convergence, a tendency to fall into local optima, and uneven distribution of the Pareto front when dealing with highly nonlinear engineering optimization problems [27–29].

To overcome the aforementioned limitations, this study aims to enhance the comprehensive dynamic performance of mining dump trucks by conducting multi-objective cooperative optimization research on hydro-pneumatic suspension parameters. First, a dynamic model of the hydro-pneumatic suspension incorporating a nonlinear valve sys-

tem model with gas–liquid coupling is established, and its accuracy is verified through bench tests. Subsequently, based on a quarter-vehicle model, the influence patterns of key structural parameters on vehicle vertical dynamic performance are systematically analyzed. On this basis, a multi-objective optimization problem for the suspension parameters is formulated, aiming to minimize the RMS values of both the sprung mass acceleration and the dynamic tire load. To address the shortcomings of the traditional MOPSO algorithm, this paper proposes an IMOPSO algorithm that integrates adaptive inertia weight, dynamic flight parameter update, and an enhanced mutation strategy, thereby improving the algorithm convergence and the distribution quality of the solution set. Finally, simulation comparisons under steady-state random road excitations and transient bump road excitations are conducted to comprehensively validate the effectiveness of the optimized suspension in improving vehicle ride comfort, wheel grounding performance, and driving safety. The main contributions of this study include the following:

(1) A high-fidelity and experimentally validated nonlinear coupled dynamic model of the hydro-pneumatic suspension is established.
(2) An improved multi-objective particle swarm optimization (IMOPSO) algorithm integrating multiple enhancement strategies is proposed.
(3) Multi-objective cooperative optimization of key suspension parameters is achieved, effectively balancing the ride comfort and wheel grounding performance of mining dump trucks.

The remainder of this paper is organized as follows. Section 2 establishes the mathematical model of the hydro-pneumatic suspension and provides experimental validation. Section 3 constructs a quarter-vehicle model and analyzes the influence patterns of key parameters. Section 4 details the formulation of multi-objective optimization problem and the design of IMOPSO algorithm. Section 5 presents an analysis of the optimization results and their verification under multiple operating conditions. Finally, Section 6 summarizes the main research conclusions.

2. Modeling of Hydro-Pneumatic Suspension

The research object of this paper is the hydro-pneumatic suspension used in mining dump trucks, and its simplified structure is shown in Figure 1a. The working principle of this suspension is as follows. When the piston rod moves, hydraulic oil flows through the damping orifice and the check valve, generating a damping force. Simultaneously, the movement of the hydraulic oil causes a volume change in the top gas chamber, thereby adjusting the system stiffness. Consequently, the hydro-pneumatic suspension can provide both stiffness and damping effects, and its total output force F can be expressed as follows:

$$F = F_c + F_k \tag{1}$$

where F_c represents the suspension damping force; F_k denotes the suspension elastic force. Next, this paper will proceed to model the suspension damping force and elastic force based on the specific structure of the hydro-pneumatic suspension, in order to construct the required system model.

2.1. Modeling of Suspension Damping Force

As shown in Figure 1b, when the hydro-pneumatic suspension is in the compression stroke, the hydraulic pressure P_1 in the piston chamber is greater than the hydraulic pressure P_2 in the annular chamber. Driven by this pressure difference, the hydraulic oil flows from the piston chamber to the annular chamber through the damping orifice and the

check valve. The total flow rate of the hydraulic oil under this condition can be calculated by the following equation:

$$Q = Q_1 + Q_2 = nC_sA_s\sqrt{\frac{2}{\rho}(P_1 - P_2)} + nC_dA_d\sqrt{\frac{2}{\rho}(P_1 - P_2)} \quad (2)$$

where ρ represents the density of the hydraulic oil; Q_1 and Q_2 denote the flow rates through the damping orifice and check valve, respectively; n represents the number of damping orifices and check valves, where $n = 1$ in this paper; C_s and C_d are the flow coefficients of the damping orifice and check valve, respectively; A_s and A_d are the effective flow areas of the damping orifice and check valve, respectively; P_1 and P_2 are the hydraulic pressures in the piston chamber and annular chamber, respectively.

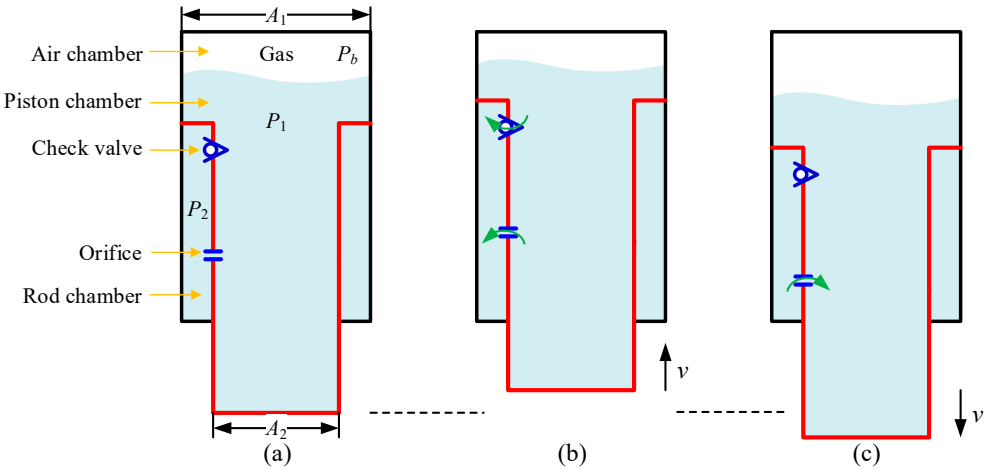

Figure 1. Hydropneumatics suspension: (**a**) structure; (**b**) compression stroke; (**c**) stretching stroke.

As shown in Figure 1c, when the hydro-pneumatic suspension is in the rebound stroke, the hydraulic pressure P_1 in the piston chamber becomes lower than the hydraulic pressure P_2 in the annular chamber. Under this condition, the check valve closes, and the hydraulic oil can only flow from the annular chamber to the piston chamber through the damping orifice. The total flow rate for this operating condition can be calculated by the following equation:

$$Q = Q_1 = nC_sA_s\sqrt{\frac{2}{\rho}(P_2 - P_1)} \quad (3)$$

By combining Equations (2) and (3), the total oil exchange flow rate between the two chambers of the hydro-pneumatic suspension during both compression and rebound strokes can be uniformly expressed in the following form:

$$Q = n\left\{C_sA_s + C_dA_d\left[\frac{1}{2} + \frac{1}{2}\text{sign}(\dot{x})\right]\right\}\sqrt{\frac{2}{\rho}\Delta p \cdot \text{sign}(\dot{x})} \quad (4)$$

where $\Delta p = p_1 - p_2$; $\dot{x}$ represents the relative velocity between the piston rod and the cylinder of the hydro-pneumatic suspension; and $\text{sign}(\cdot)$ denotes the sign function, which is defined as follows:

$$\text{sign}(\dot{x}) = \begin{cases} 1, & \dot{x} \geq 0 \\ -1, & \dot{x} < 0 \end{cases} \quad (5)$$

Assuming the hydraulic oil is incompressible, we have the following:

$$Q = (A_1 - A_2)\dot{x} \quad (6)$$

where A_1 denotes the cross-sectional area of the piston and A_2 represents the effective cross-sectional area of the piston rod.

By combining Equations (4) and (6), we have

$$n\left\{C_s A_s + C_d A_d\left[\frac{1}{2} + \frac{1}{2}\mathrm{sign}(\dot{x})\right]\right\}\sqrt{\frac{2}{\rho}\Delta p \cdot \mathrm{sign}(\dot{x})} = (A_1 - A_2)\dot{x} \tag{7}$$

By squaring both sides of Equation (7) and simplifying, we obtain

$$\Delta p = \frac{\rho(A_1 - A_2)^2 \dot{x}^2 \cdot \mathrm{sign}(\dot{x})}{2n^2\left\{C_s A_s + C_d A_d\left[\frac{1}{2} + \frac{1}{2}\mathrm{sign}(\dot{x})\right]\right\}^2} \tag{8}$$

Then, the damping force F_c of hydro-pneumatic suspension can be obtained as:

$$F_c = \Delta p \cdot \Delta A = \frac{\rho(A_1 - A_2)^3 \dot{x}^2 \cdot \mathrm{sign}(\dot{x})}{2n^2\left\{C_s A_s + C_d A_d\left[\frac{1}{2} + \frac{1}{2}\mathrm{sign}(\dot{x})\right]\right\}^2} \tag{9}$$

where $\Delta A = A_1 - A_2$.

2.2. Modeling of Suspension Spring Force

At the initial equilibrium state, the hydro-pneumatic suspension remains stationary under the action of the sprung mass m_s. Assuming the gas chamber volume at this position is V_0 and the gas pressure is P_0, the following relationship holds:

$$P_0 = \frac{m_s g}{A_2} \tag{10}$$

where $P_0 = P_1$; and g denotes the acceleration due to gravity.

Considering that the changes in gas temperature and pressure during the operation of the hydro-pneumatic suspension are not significant, the process can be simplified as isothermal in the analysis. Based on the ideal gas isothermal assumption, we have the following relation:

$$P_b V_b^r = P_0 V_0^r \tag{11}$$

where P_b represents the instantaneous gas pressure during the operation of the suspension; V_b denotes the gas volume; and r refers to the polytropic exponent of the gas.

During the operation of the suspension, the variation in gas volume can be expressed as follows:

$$V_b = V_0 - A_2 x \tag{12}$$

Therefore, the expression for the elastic force F_k of the hydro-pneumatic suspension can be derived as follows:

$$F_k = P_b A_2 = \frac{P_0 V_0^r A_2}{(V_0 - A_2 x)^r} \tag{13}$$

Considering the relationship between the gas chamber volume V_0 at the equilibrium state and the initial gas-filled height h_0, we have

$$V_0 = A_1 h_0 \tag{14}$$

where h_0 represents the initial gas charging height of the hydro-pneumatic suspension.

The elastic force of the hydro-pneumatic suspension can be further expressed as follows:

$$F_k = \frac{m_s g}{\left(1 - \frac{A_2 x}{A_1 h_0}\right)^r} \tag{15}$$

2.3. Modeling of Total Output Force

By combining Equations (1), (9) and (15), the total output force of the hydro-pneumatic suspension can be expressed as follows:

$$F = \frac{\rho(A_1 - A_2)^3 \dot{x}^2 \cdot \mathrm{sign}(\dot{x})}{2n^2\left\{C_s A_s + C_d A_d\left[\frac{1}{2} + \frac{1}{2}\mathrm{sign}(\dot{x})\right]\right\}^2} + \frac{m_s g}{\left(1 - \frac{A_2 x}{A_1 h_0}\right)^r} \tag{16}$$

The specific structure of the damping orifice and check valve for this hydro-pneumatic suspension is shown in Figure 2. It can be observed that the length of this damping orifice is significantly greater than its diameter, which allows it to be considered as a thin-walled orifice. Thus, based on Bernoulli's orifice flow equation, its effective flow area can be expressed as follows:

$$A_s = \frac{1}{4}\pi d_0^2 \tag{17}$$

where d_0 represents the damping orifice diameter.

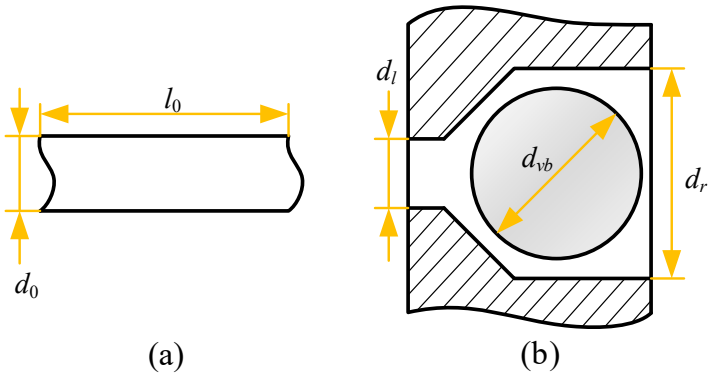

Figure 2. Damping hole and check valve structure: (**a**) damping hole; (**b**) check valve.

The check valve features a horizontally symmetrical configuration. When the steel ball opens, the flow area of the check valve is primarily constrained by the valve seat hole. Due to the high hydraulic pressure, the valve opens and closes rapidly, allowing its state to be approximated as either "fully closed" or "fully open." When it is fully open, it can be approximated as a damping hole and its effective flow area can be expressed as follows:

$$A_d = \frac{1}{4}\pi d_{v1}^2 \tag{18}$$

where d_{v1} represents the equivalent check valve seat hole diameter.

2.4. Validation of Hydro-Pneumatic Suspension Model

Based on the established mathematical model and using the initial system parameters listed in Table 1 for simulation, Figure 3 presents the variation curves of the damping force, elastic force, and total output force of the hydro-pneumatic suspension with respect to its relative motion velocity. The parameters presented in Table 1 were determined experimentally. Key physical dimensions were measured directly from the hydro-pneumatic suspension prototype. As shown in the figure, with increasing suspension displacement,

the output force exhibits a clear nonlinear growth trend due to the influence of nonlinear factors such as gas compressibility and the fluid flow in the valve system. Unlike traditional suspensions, which require separate configurations of springs and dampers, the hydro-pneumatic suspension inherently generates an elastic force that varies nonlinearly with displacement. Furthermore, since the check valve opens only during the compression stroke, the damping force of the hydro-pneumatic suspension exhibits asymmetry between compression and rebound. It is precisely due to this on–off characteristic of the check valve that the suspension can effectively absorb road impacts during compression by utilizing the high-pressure gas while rapidly attenuating vibrations transmitted to the vehicle body during the rebound stroke.

Table 1. Parameters of hydro-pneumatic suspension model.

Parameters (Symbol)	Value (Unit)	Parameters	Value (Unit)
Fluid density (ρ)	850 (kg/m^3)	Equivalent check valve seat hole diameter (d_{v1})	8 (mm)
Equivalent check valve seat hole diameter (d_1)	190 (mm)	Flow coefficient (C_s and C_d)	0.65
Piston rod outer diameter (d_2)	150 (mm)	Initial gas charging height (h_0)	80 (mm)
Damping orifice diameter (d_0)	12 (mm)	Maximum stroke (x_{max})	135 (mm)

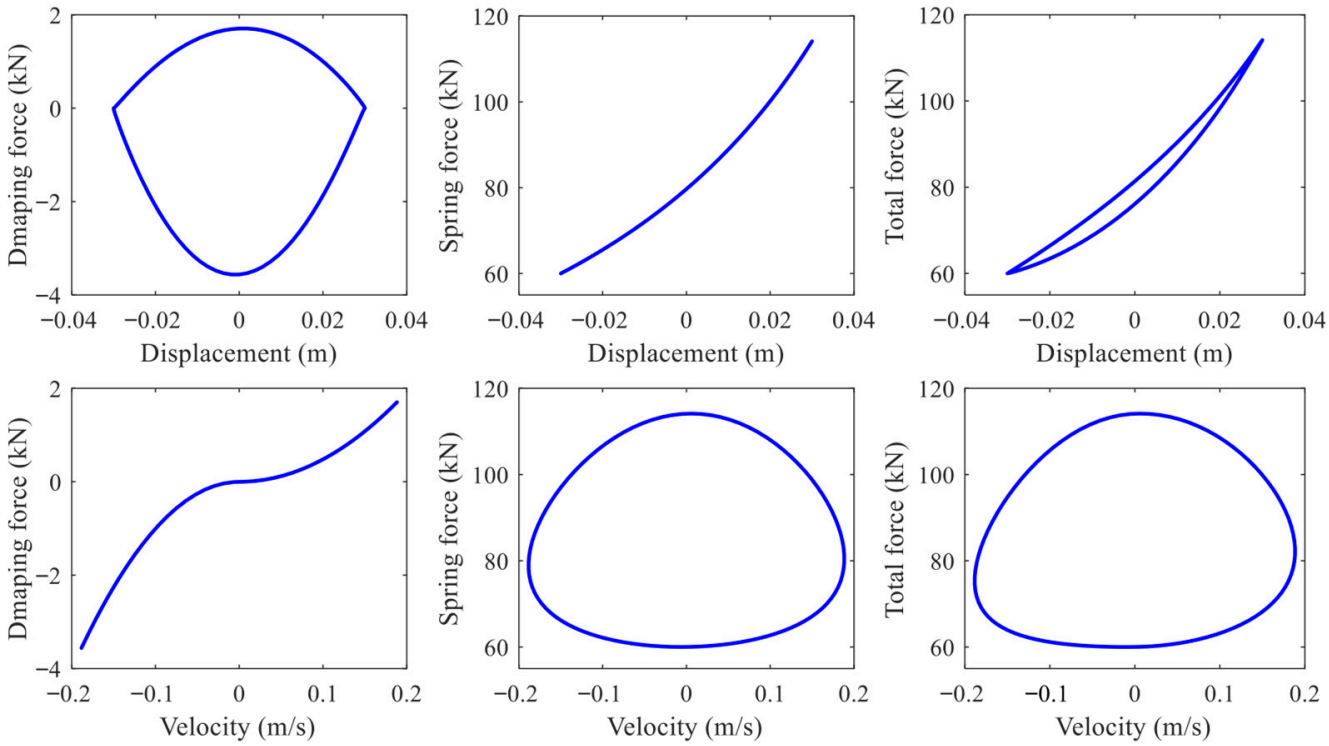

Figure 3. Force output characteristics of hydro-pneumatic suspension.

To validate the effectiveness of the established hydro-pneumatic suspension model, a corresponding characteristic test bench was constructed and experiments were conducted. The test bench primarily consists of a shock absorber test rig, a controller, a data acquisition system, a gas-charging device, and relevant sensors. The specific setup is illustrated in Figure 4a. The hydro-pneumatic suspension is vertically installed on the test bench via its upper and lower mounting lugs. Its output force and displacement signals are acquired in real time by the force sensor and displacement sensor integrated on the exciter head. During the test, the piston rod equilibrium position was set at 60 mm extension, with the internal gas pressure of the hydro-pneumatic suspension adjusted to 4.5 MPa at this state.

A sinusoidal excitation with an amplitude of 30 mm and a frequency of 1 Hz was applied to the suspension. The resulting experimental output force is compared with the simulation in Figure 4b. As illustrated in the figure, the experimental results show good agreement with the simulation results, indicating that the constructed hydro-pneumatic suspension model is correct and possesses high accuracy. It should be noted that a minor discrepancy exists between the experimental and simulation curves at the upper and lower extreme points, which is primarily attributed to the neglect of friction between the piston rod and the cylinder in this study.

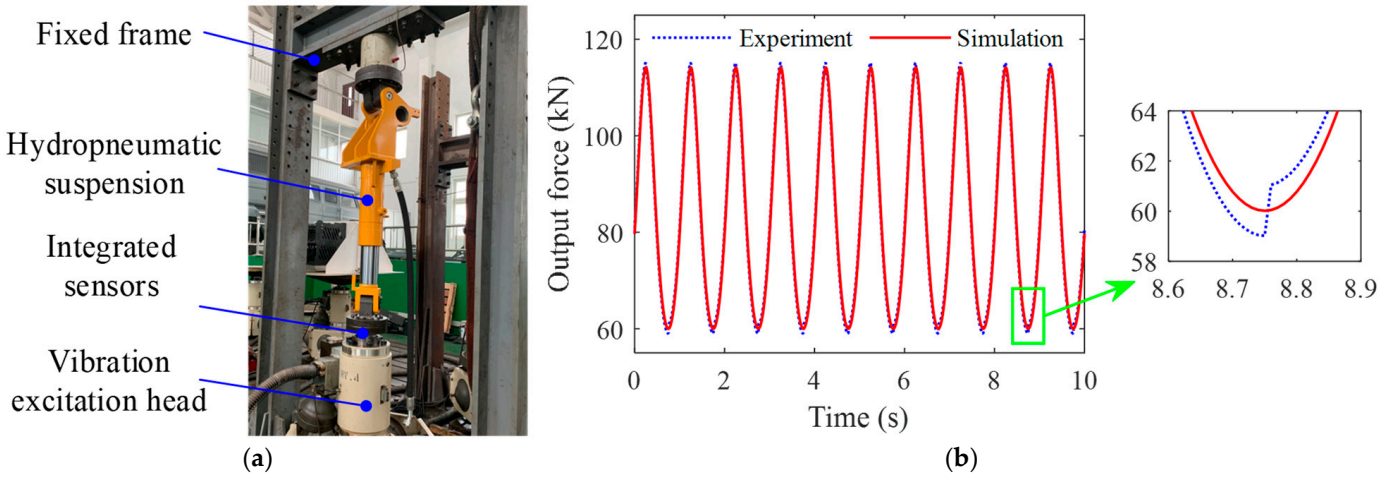

Figure 4. Comparison of simulation and experiment results: (**a**) test bench; (**b**) experimental results.

3. Suspension Parameter Influence Analysis

3.1. Quarter Vehicle Hydro-Pneumatic Suspension Model

To analyze the influence of structural parameters of the hydro-pneumatic suspension on vehicle dynamic response, a quarter-vehicle hydro-pneumatic suspension system model, as shown in Figure 5, is established in this paper. Although this model is a simplified structure, it can effectively reflect the vertical dynamic characteristics of the vehicle. A key distinction from the traditional linear quarter-car model is that all forces generated by the suspension system, including the elastic force and the damping force, are uniformly described by the nonlinear hydro-pneumatic suspension model established in Section 2 and are collectively represented as the total output force F. Additionally, tire damping is neglected, which is a common simplification justified by its typically minor magnitude relative to tire stiffness and its limited effect on the low-frequency dynamics of primary interest in this study. Based on Newton's second law, the system dynamic differential equations can be formulated as follows:

$$\begin{cases} m_s\ddot{x}_s + F = 0 \\ m_u\ddot{x}_u + k_t(x_u - x_r) - F = 0 \end{cases} \tag{19}$$

where $m_s = 8123.5$ kg represents the sprung mass; $m_u = 1669.5$ kg denotes the unsprung mass; $\ddot{x}_s$ and $\ddot{x}_u$ correspond to the displacements of the sprung and unsprung masses, respectively; $k_t = 2,800,000$ N/m represents the tire stiffness; x_r denotes the road elevation input; and in this study, a filtered white-noise method is employed to construct a random road excitation model [30], expressed as follows:

$$\dot{x}_r(t) = -2\pi f_0 v x_r(t) + 2\pi n_0 \sqrt{G_q(n_0)v} \cdot w(t) \tag{20}$$

where $f_0 = 0.011$ Hz represents the lower cut-off frequency; $n_0 = 0.1$ m^{-1} denotes the reference spatial frequency; v is the vehicle forward speed; $G_q(n_0)$ indicates the road roughness coefficient, which is related to the road roughness grade; and $w(t)$ represents zero-mean white noise.

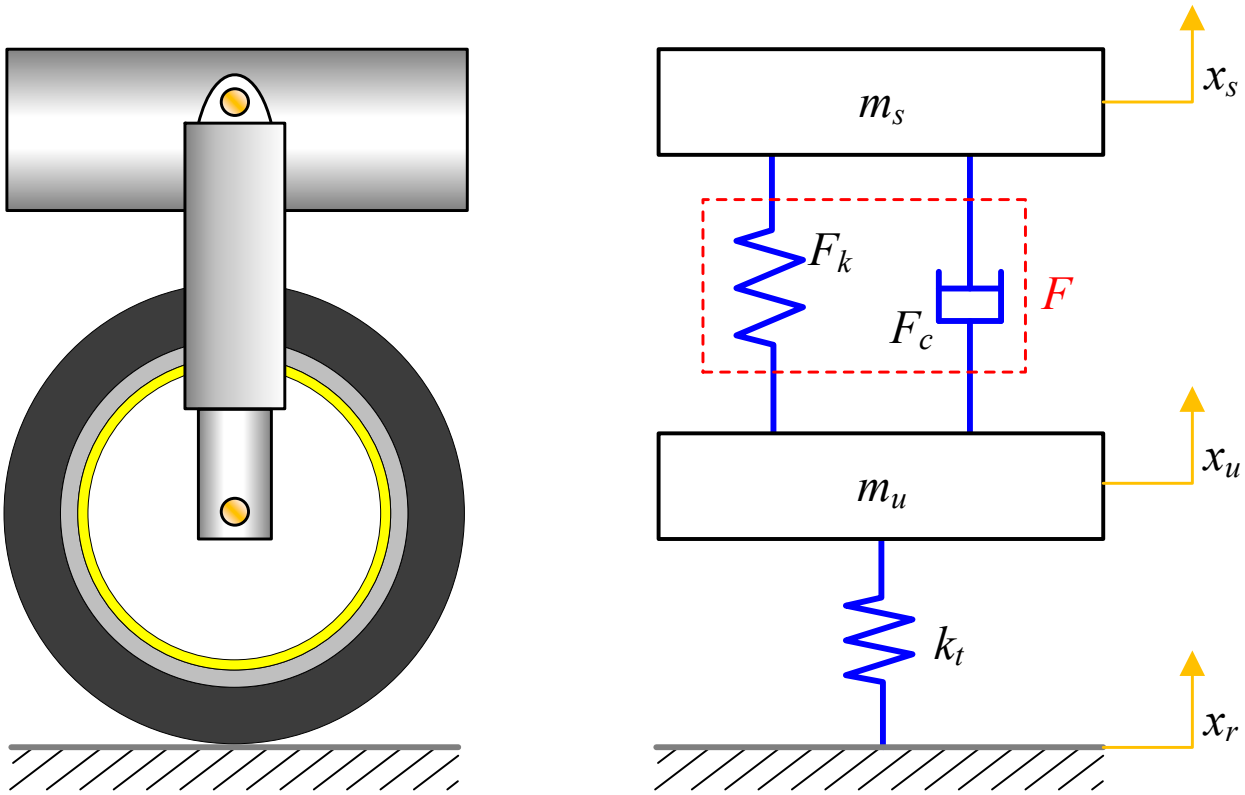

Figure 5. Quarter-vehicle hydro-pneumatic suspension model.

3.2. Influence of Suspension Parameters on Vehicle Performance

As shown in Equations (16)–(18), the output force of the hydro-pneumatic suspension is primarily influenced by the parameters A_1, A_2, d_0, d_{v1} and h_0. Among these, A_1 and A_2 are external structural parameters and are generally not considered as optimization variables in the design process. Therefore, this paper focuses on investigating the effects of the three parameters, d_0, d_{v1} and h_0, on vehicle performance, and subsequently aims to enhance the dynamic performance of the vehicle by optimizing these parameters.

Figure 6 illustrates the influence patterns of key structural parameters of the hydro-pneumatic suspension on its performance. Specifically, Figure 6a shows the effect of the damping orifice diameter d_0 on the damping characteristics. As d_0 increases, the damping force rises significantly, with a particularly sharp increase observed during the rebound stroke, which further strengthens the asymmetric nature of the damping force. While a higher rebound damping helps improve wheel grounding performance, it may also compromise ride comfort to some extent. Figure 6b illustrates the influence of the equivalent check valve seat hole diameter d_{v1} on the damping characteristics. The parameter d_{v1} primarily affects the damping behavior when the velocity is greater than zero (compression stroke), while its impact is negligible when the velocity is less than zero (rebound stroke). This occurs because the check valve remains closed during the rebound stroke, rendering changes in d_{v1} inactive. In contrast, during the compression stroke where the check valve opens, an increase in d_{v1} enlarges the flow area, thereby significantly reducing the damping force. Figure 6c illustrates the influence of the initial gas charging height h_0 on the suspension stiffness. As h_0 increases, the nonlinear stiffness of the system decreases

significantly, with the rate of stiffness reduction being much higher during the compression stroke compared to the rebound stroke.

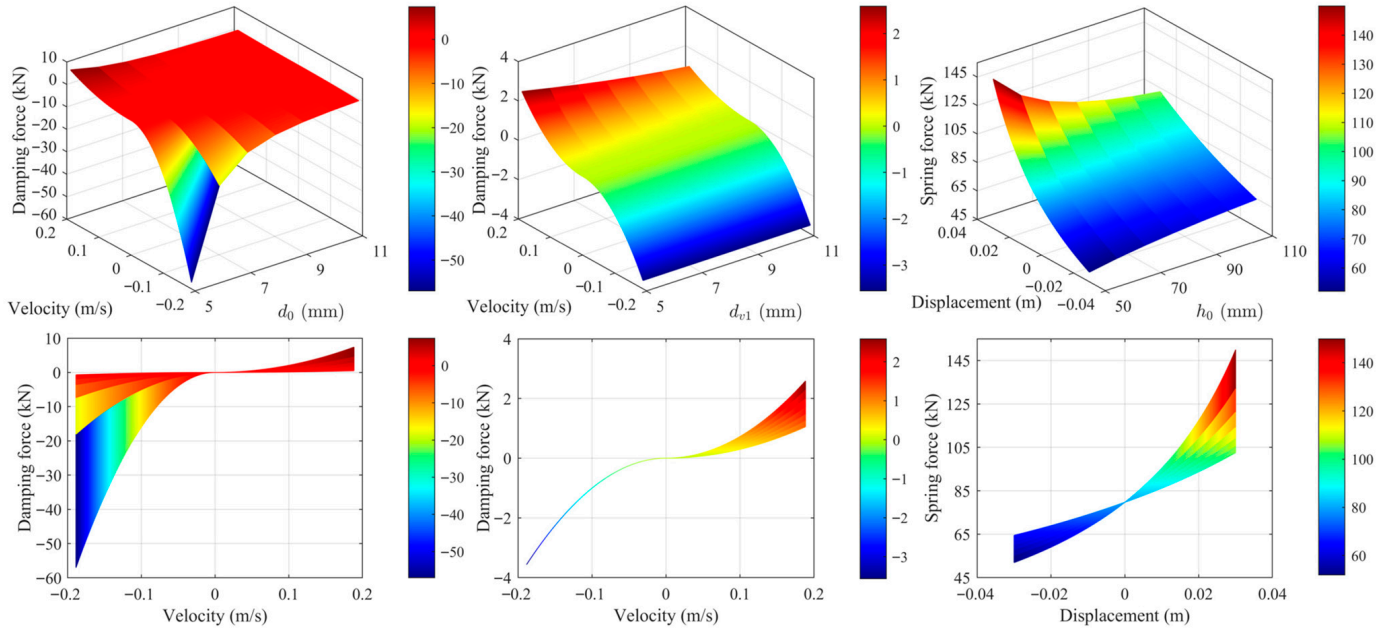

(**a**) (**b**) (**c**)

Figure 6. Parameter influence analysis: (**a**) effect of d_0 on damping force; (**b**) effect of d_{v1} on damping force; (**c**) effect of h_0 on spring force.

Based on the analysis above, this paper further investigates the influence of the structural parameters of the hydro-pneumatic suspension on the overall vehicle dynamic performance. Figure 7 presents the normalized results of various vehicle performance indicators as the parameters d_0, d_{v1} and h_0 vary. As shown in Figure 7a, as the damping orifice diameter d_0 increases, the sprung mass acceleration, suspension rattle space, and dynamic tire load all exhibit a trend of initially decreasing and then increasing. Among these, the ride comfort and wheel grounding performance reach their optimal levels when d_0 is approximately 0.8 times the initial design value. Figure 7b indicates that an increase in the valve seat hole diameter d_{v1} leads to a continuous rise in all three aforementioned performance metrics, meaning the overall performance gradually deteriorates. Therefore, to achieve better vehicle dynamic performance, d_{v1} should be selected as small as possible within the feasible range. Figure 7c illustrates the influence pattern of the initial gas charging height h_0. As h_0 increases, the sprung mass acceleration, suspension rattle space, and dynamic tire load first increase and then decrease. Although a higher h_0 is beneficial for improving ride comfort and wheel grounding performance, its value cannot be excessively large due to constraints imposed by engineering layout and sealing requirements. A comprehensive review of Figure 7a–c further reveals that among the three structural parameters, the damping orifice diameter d_0 exerts the most pronounced impact on the overall vehicle performance. Moreover, the influence of each parameter on different performance metrics often exhibits consistent or conflicting relationships, making it difficult to determine an optimal value through a single objective directly. Therefore, this paper will undertake a coordinated design and comprehensive optimization of these three parameters from a multi-objective optimization perspective.

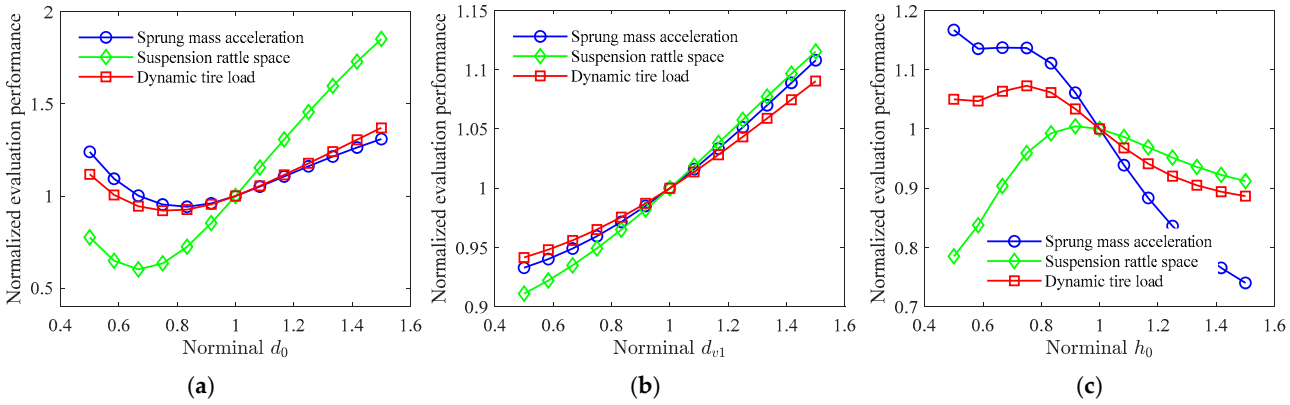

Figure 7. Effects of different parameters on vehicle performances: (**a**) d_0; (**b**) d_{v1}; (**c**) h_0.

4. Multi-Objective Optimization Method for Hydro-Pneumatic Suspension Parameters

4.1. Formulation of Multi-Objective Optimization Problems

This study aims to enhance both vehicle ride comfort and wheel grounding performance simultaneously by optimizing the key parameters of the hydro-pneumatic suspension. This problem falls into the category of a typical multi-objective optimization problem, where ride comfort is evaluated by the RMS value of the sprung mass acceleration, and wheel grounding performance is assessed by the RMS value of the dynamic tire load. Accordingly, the optimization objectives are defined as follows:

$$\begin{cases} f_1(\mathbf{x}) = \sigma_{\ddot{z}_s} \\ f_2(\mathbf{x}) = \sigma_{Fd} \end{cases} \tag{21}$$

where $\sigma_{\ddot{z}_s}$ and σ_{Fd} denote the RMS values of the sprung mass acceleration and the dynamic tire load, respectively, with specific calculation methods referenced in the literature [31], and $\mathbf{x}$ represents the optimization variables. The structural parameters to be optimized in this study mainly include the damping orifice diameter d_0, the valve seat hole diameter d_{v1}, and the initial gas charging height h_0. Therefore, the variable vector can be expressed as $\mathbf{x} = \begin{bmatrix} d_0 & d_{v1} & h_0 \end{bmatrix}^{\mathrm{T}}$.

To improve ride comfort, the RMS value of the sprung mass acceleration needs to be minimized. Simultaneously, to enhance wheel grounding performance, the RMS value of the dynamic tire load must also be minimized. This multi-objective optimization problem can be formulated as follows:

$$\min F(\mathbf{x}) = \{f_1(\mathbf{x}), f_2(\mathbf{x})\} \tag{22}$$

where $F(\mathbf{x})$ denotes the objective function.

During the solution process of the optimization problem, practical engineering feasibility must be fully considered to ensure all optimization variables remain within their feasible ranges. First, the suspension rattle space must be less than its maximum working stroke to prevent the vehicle from contacting the limit blocks during operation, thereby ensuring safety and reliability. Second, the variation range of each optimization parameter is limited to 0.3 to 1.7 times its initial design value, balancing practical engineering feasibility with an adequate optimization margin. In summary, the constraints of this optimization problem can be formulated as follows:

$$\begin{cases} \Delta x \le x_{\max} \\ d_{0_\min} \le d_0 \le d_{0_\max} \\ d_{v1_\min} \le d_{v1} \le d_{v1_\max} \\ h_{0_\min} \le h_0 \le h_{0_\max} \end{cases} \tag{23}$$

where $\Delta x = x_s - x_u$ represents the suspension rattle space; $x_{\max}$ = 0.065 mm denotes the maximum allowable suspension stroke; $d_{0_\min}$, $d_{v1_\min}$ and $h_{0_\min}$ represent the lower bounds of the respective optimization variables, each set at 0.3 times its corresponding initial design value; and conversely, $d_{0_\max}$, $d_{v1_\max}$ and $h_{0_\max}$ represent the upper bounds, each set at 1.7 times its corresponding initial design value.

4.2. Design of IMOPSO Algorithm

To solve the aforementioned multi-objective optimization problem, this paper employs the widely used MOPSO algorithm. However, the traditional MOPSO algorithm still exhibits shortcomings in terms of convergence rate, global exploration capability, and population diversity, which may affect the distribution quality and convergence efficiency of the Pareto front. Therefore, this paper proposes an IMOPSO algorithm that integrates multiple strategies.

First, to address the issue that the traditional MOPSO algorithm is prone to local optima due to its fixed inertia weight, this paper introduces an adaptive inertia weight adjustment mechanism based on population diversity. This method dynamically perceives the distribution differences in the fitness of the particle swarm and adaptively adjusts the inertia weight. Specifically, when the fitness diversity among the particles is high, the inertia weight is increased to promote global exploration. Conversely, when the fitness diversity is low, the inertia weight is decreased to enhance local exploitation, thereby accelerating algorithm convergence while improving the quality of the solution set. The adaptive update rule for the inertia weight is formulated as follows:

$$\omega = \begin{cases} \omega_{\max}\left(1 - \frac{t_c}{t_{\max}}\right), & f_{\text{diff}} \ge \delta_\omega \\ \omega_{\min} + (\omega_{\max} - \omega_{\min}) \exp\left(-0.1 \times \frac{t_c}{t_{\max}}\right), & \text{else} \end{cases} \tag{24}$$

where δ_ω denotes the adjustment threshold for the inertia weight ω, set here as $\delta_\omega = 0.3$; t_c and $t_{\max}$ represent the current iteration count and the maximum iteration count, respectively; and f_{diff} refers to the fitness difference.

Second, to further balance the algorithm capability between global exploration and local exploitation, this paper designs a dynamic flight parameter update strategy. In particle swarm optimization algorithms, the flight parameters (namely the cognitive coefficient c_1 and the social coefficient c_2) directly influence how particles update their states based on their personal best positions and the global best position of the swarm. To this end, this paper dynamically adjusts c_1 and c_2 according to the distance relationship between the particle current position and its personal best and the global best, as well as the difference between the particle fitness and the average fitness of the swarm. The initial update formula for a particle is given as follows:

$$\begin{cases} c_1 = \alpha_1 \times \text{Sigmoid}(d_p) + \beta_1 \\ c_2 = \alpha_2 \times \text{Sigmoid}(d_g) + \beta_2 \end{cases} \tag{25}$$

where d_p and d_g denote the Euclidean distances from the particle to its personal best solution and the global best solution, respectively; α_1, α_2, β_1 and β_2 represent the corresponding adjustment coefficients.

When the particle fitness is relatively poor, indicating that its current fitness f_{cur} exceeds the average fitness f_{avg} of the swarm, the coefficients c_1 and c_2 are appropriately increased to enhance global exploration. Conversely, when the particle fitness is favorable, meaning its current fitness is below the swarm average fitness, c_1 and c_2 are correspondingly reduced to promote local refinement. Based on this strategy, the dynamic update rules for c_1 and c_2 are designed as follows:

$$\begin{cases} c_1 = c_1 + \gamma_c \times (f_{\text{cur}} - f_{\text{avg}}) \\ c_2 = c_2 + \gamma_c \times (f_{\text{cur}} - f_{\text{avg}}) \end{cases} \tag{26}$$

where γ_c represents the adjustment factor.

To further enhance the algorithm capability to escape local optima, this paper improves the conventional mutation strategy and introduces an adaptive mutation mechanism. This mechanism addresses the limitations of a fixed mutation rate, which cannot be dynamically adjusted during iterations and often fails to balance exploration and exploitation effectively, thus improving the overall optimization performance of the algorithm. The expression for the adaptive mutation mechanism is given as follows:

$$p_{\text{cur}} = \sqrt[\eta]{1 - \frac{t_c - 1}{t_{\max} - 1}} \tag{27}$$

where p_{cur} represents the current mutation probability and η denotes the adjustment coefficient for mutation rate.

5. Analysis and Verification of Optimization Results

5.1. Analysis and Discussion of Optimization Results

The flowchart of the hydro-pneumatic suspension parameter optimization based on the IMOPSO algorithm is shown in Figure 8. The specific steps are as follows:

(1) Define the fitness function and complete parameter initialization. Establish a non-dominated solution archive, construct an adaptive grid structure, and configure the initial grid indices.

(2) Dynamically update the inertia weight and learning factors to adjust the velocity and position of each particle. Evaluate the distribution characteristics of the solution set by calculating the multi-scale crowding degree, and based on this, select the leader particles that guide the swarm evolution.

(3) Re-evaluate the particle fitness. Perform mutation operations when specific conditions are met to enhance the exploration capability and diversity of the swarm. Subsequently, update the personal best solutions, record the changes in fitness, and adaptively adjust the inertia weight accordingly.

(4) Update the dominance relationships within the archive. If the archive size exceeds the preset limit, employ a roulette-wheel-based selection strategy for reduction. After each iteration, update the grid and its indices accordingly. Repeat the above process until the preset maximum number of iterations is reached, and finally, output the optimal solution set.

To validate the effectiveness and superiority of the proposed IMOPSO algorithm, this study selected the classical MOPSO algorithm and the NSGA-II algorithm as benchmarks. A test set comprising both unimodal and multimodal functions was employed for comparative performance evaluation. The functions utilized are as follows:

$$\begin{cases} f_{t1}(x) = \sum_{i=1}^{m} x_i^2 + \left(\frac{1}{2}\sum_{i=1}^{m} ix_i\right)^2 + \left(\frac{1}{2}\sum_{i=1}^{m} ix_i\right)^4, x \in [-5,5] \\ f_{t2}(x) = \frac{1}{4000}\sum_{i=1}^{m} x_i^2 - \prod_{i=1}^{m} \cos\left(\frac{x_i}{\sqrt{i}}\right) + 1, x \in [-3,1] \end{cases} \quad (28)$$

where m denotes the search dimension.

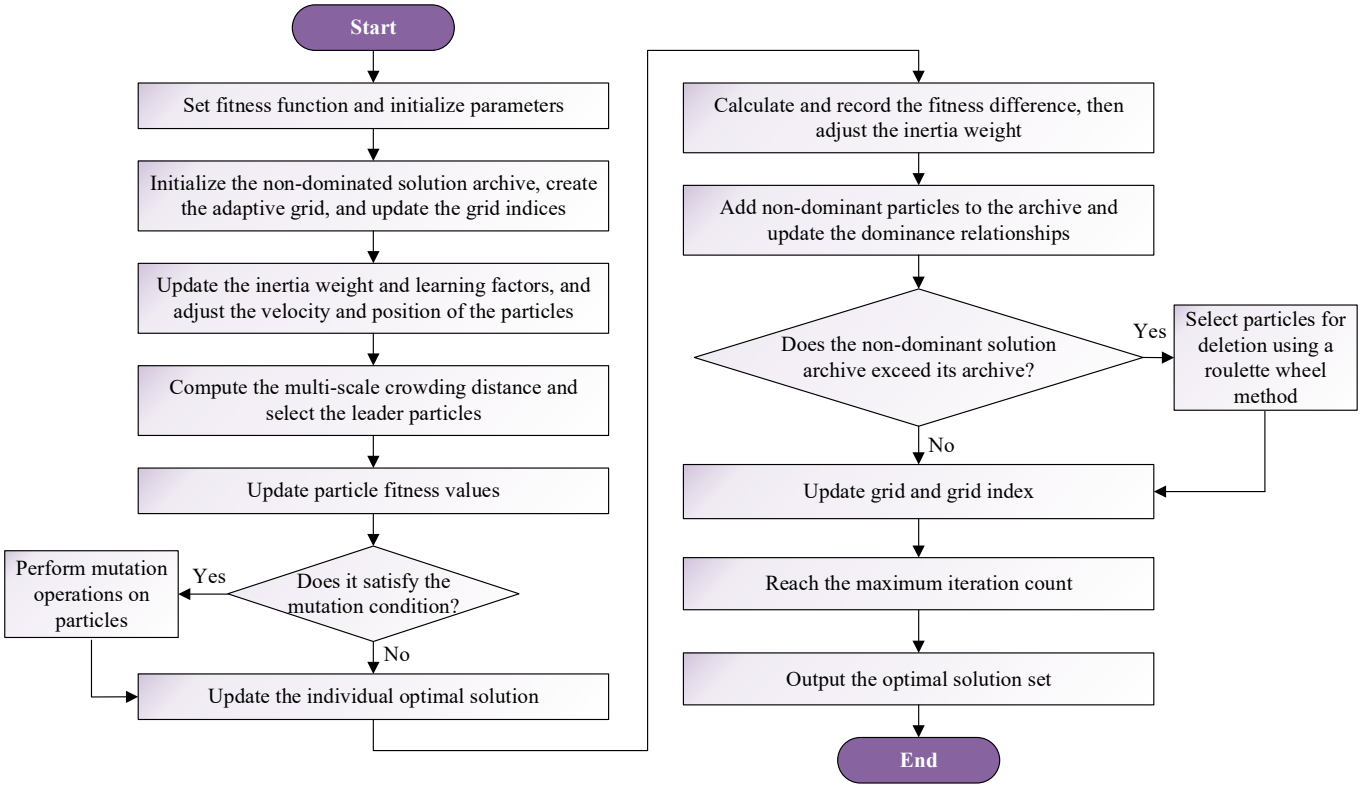

Figure 8. IMOPSO algorithm optimization process.

The experimental setup was designed as follows, where the search dimension is 30. To mitigate the influence of randomness, each algorithm was executed independently for 30 runs, with the maximum number of iterations set to 300 per run. The best value, the mean value, and the standard deviation obtained from these 30 runs were recorded as the performance metrics. The detailed results are presented in Table 2. The parameter configuration used for the proposed IMOPSO algorithm in this study is provided in Table 3.

Table 2. Comparison of algorithm performance test results.

Algorithm	Statistical Value	f_{t1}	f_{t2}
IMOPSO	Best value	0	0
	Mean value	0	0
	Standard deviation	0	0
MOPSO	Best value	7.59×10^{-9}	0
	Mean value	5.70×10^{-21}	0
	Standard deviation	3.63×10^{-20}	3.12×10^{-2}
NSGA-II	Best value	1.66×10^{-12}	0
	Mean value	7.58×10^{-9}	4.17×10^{-3}
	Standard deviation	1.88×10^{-8}	8.09×10^{-3}

Table 3. Parameter settings for the IMOPSO algorithm.

Parameter	ω_{min}	ω_{max}	α_1	α_2	β_1	β_2	γ_c	η	t_{max}
Value	0.3	0.9	1.5	1.0	1.0	2.0	0.1	0.1	300

The experimental results demonstrate that on test functions f_{t1} and f_{t2}, the proposed IMOPSO algorithm consistently achieved the optimal solution across all 30 independent runs. Its best value, mean value, and standard deviation were all zero. This indicates that IMOPSO not only converges stably to the theoretical optimum but also exhibits strong convergence accuracy and robustness, with no performance variation observed between different runs. In comparison, the MOPSO algorithm attained a near-optimal solution on f_{t1} (best value 7.59×10^{-9}), yet its mean performance and standard deviation reveal weaker convergence stability, especially on f_{t2} where noticeable fluctuation occurred (standard deviation 3.12×10^{-2}). The NSGA-II algorithm also achieved a relatively good best value on f_{t1} (1.66×10^{-12}), but its average convergence accuracy was significantly lower than that of IMOPSO. Moreover, the mean and standard deviation on f_{t2} suggest a more scattered distribution of solutions, reflecting inferior convergence stability and consistency compared to IMOPSO. Overall, IMOPSO exhibits markedly better convergence performance and operational stability than the conventional MOPSO and NSGA-II on the selected test problems. The zero-deviation and zero-variance outcomes confirm that the algorithm effectively overcomes the influence of random initialization and possesses strong global convergence capability and algorithmic reliability.

To this end, the proposed IMOPSO algorithm was employed to optimize the key parameters of the hydro-pneumatic suspension. This multi-objective optimization problem involves three design variables, i.e., the optimization dimension is 3. The quarter-vehicle model from Equation (19) served as the evaluation model during the optimization, which was performed under class-C road excitation. This process yielded the Pareto optimal front shown in Figure 9.

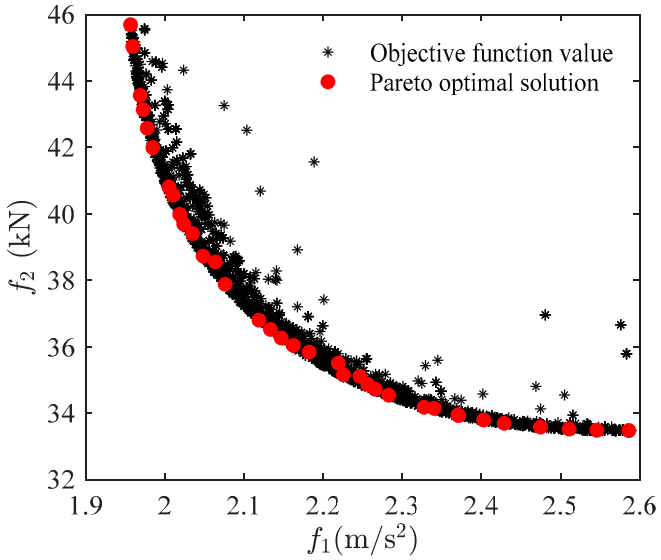

Figure 9. Pareto frontier solution set of the optimization problem.

Figure 9 reveals a significant trade-off relationship between vehicle ride comfort and wheel grounding performance. Although ride comfort can be improved to a certain extent by appropriately selecting the hydro-pneumatic suspension parameters, this often leads to a degradation in wheel grounding performance, and vice versa. This indicates that within the

parameter design frontier, there exists no single set of parameters that can simultaneously outperform all other combinations in terms of both ride comfort and handling performance. To enhance ride comfort as much as possible while ensuring wheel grounding performance, this study adopts a balanced solution that takes both aspects into consideration, specifically assigning a weight of 70% to ride comfort and 30% to wheel grounding performance. A comparison of the hydro-pneumatic suspension parameters before and after optimization is presented in Table 4. It can be observed that the optimization results are consistent with the conclusions drawn from the parameter analysis. To achieve better vehicle dynamic performance, the check valve seat hole diameter d_{v1} and the initial gas charging height h_0 are set to the minimum and maximum allowable values within their respective feasible ranges. Furthermore, a reasonable value is selected for the damping orifice diameter d_0 to achieve a favorable balance between ride comfort and wheel grounding performance.

Table 4. Parameter optimization results.

Parameters	Value	
	Before Optimization	**After Optimization**
Damping orifice diameter (d_0)	12 mm	13.8 mm
Equivalent check valve seat hole diameter (d_{v1})	8 mm	2.4 mm
Initial gas charging height (h_0)	80 mm	136 mm

Figure 10 compares the dynamic response characteristics of the hydro-pneumatic suspension before and after parameter optimization. The results indicate that both the damping and stiffness characteristics of the optimized suspension undergo significant changes. Specifically, the change in damping characteristics during the compression stroke is relatively limited, whereas the damping coefficient shows a notable decrease during the rebound stroke. This configuration with lower damping contributes to improved ride comfort of the vehicle. Meanwhile, the suspension stiffness coefficient is also significantly reduced after optimization. Under the premise of ensuring adequate load-carrying capacity, a lower stiffness helps reduce body vibrations, thereby further enhancing ride comfort.

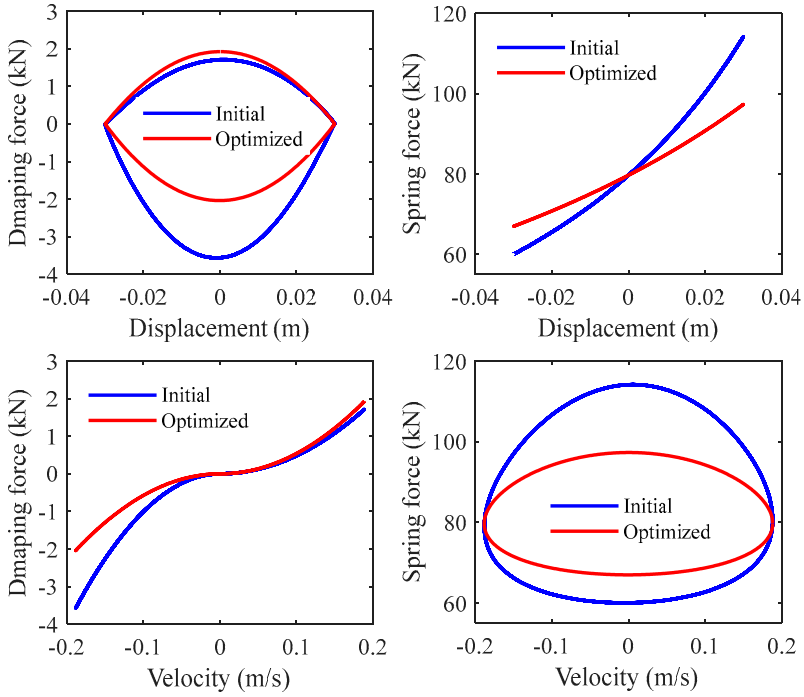

Figure 10. Force output characteristics before and after optimization.

5.2. Comprehensive Verification of Optimization Performance

To further validate the effectiveness of the parameter optimization results and the superiority of the optimized hydro-pneumatic suspension in enhancing overall vehicle performance, comparative simulations were conducted under both steady-state random road and transient bump road excitations. The simulation results under class-C road excitations are shown in Figure 11, with the vehicle speed maintained at 10 m/s throughout the simulation.

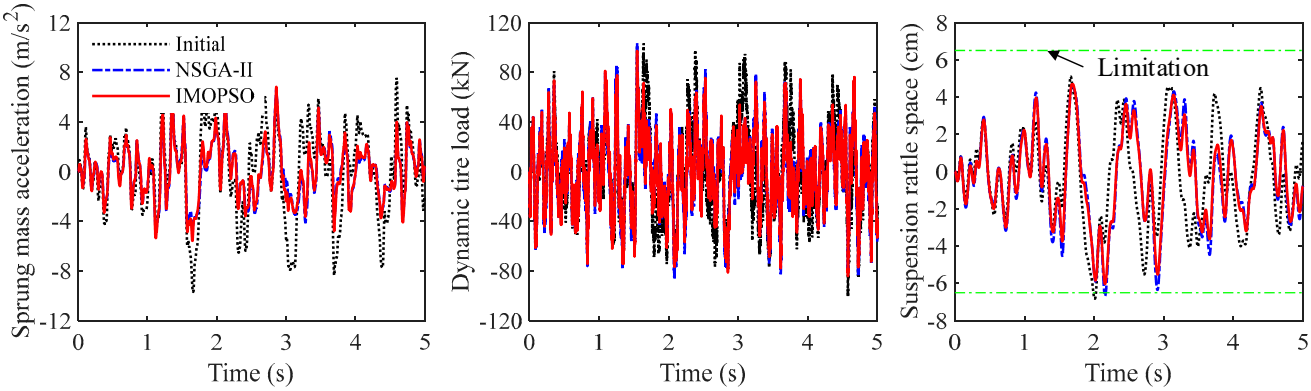

Figure 11. Comparison of vehicle dynamic performance on class-C roads.

As illustrated in Figure 11, under class C road excitation, both optimization algorithms significantly improve the vehicle dynamic performance compared to the initial parameters. Specifically, the curves obtained after optimization using IMOPSO and NSGA-II exhibit smaller fluctuations in both the sprung mass acceleration and the dynamic tire load, indicating enhanced ride comfort and wheel grounding performance. Meanwhile, the suspension rattle space is effectively constrained within the allowable travel range, thereby avoiding contact with the limit blocks. To analyze the frequency characteristics of the suspension dynamic response, a fast Fourier transform was applied to the time-domain results, and the frequency-domain comparison is shown in Figure 12. It can be observed that both optimization algorithms demonstrate notable frequency selectivity. In the critical frequency band related to comfort and safety, namely around the body resonance frequency of approximately 1 Hz, both IMOPSO and NSGA-II effectively suppress the resonance peaks of the sprung mass acceleration and the dynamic tire load. This indicates that the optimization algorithms successfully adjust the impedance characteristics of the suspension system against body-dominant vibrations. However, in the wheel resonance frequency band and higher frequency ranges, the optimization effect is limited, and the dynamic tire load response even slightly deteriorates, suggesting potential directions for further improvement.

The quantitative comparison of RMS values in Table 5 clearly reveals the superiority of the IMOPSO algorithm in overall performance. Regarding the core safety and comfort indicators, IMOPSO either achieves the best performance or shows an extremely balanced result. IMOPSO reduces the RMS value of the dynamic tire load to 30.584 kN, which is below the safety threshold of one-third of the static wheel load [$1/3 \cdot (m_s + m_u) \cdot g = 32.023$ kN], representing a reduction of 15.8%. This performance surpasses that of NSGA-II, which reduces the value to 31.715 kN, a reduction of 12.7%. This demonstrates that the IMOPSO-optimized solution can more effectively ensure wheel grounding performance, directly enhancing driving safety. At the same time, its reduction in sprung mass acceleration (37.6%) is comparable to the excellent level achieved by NSGA-II (39.8%), significantly improving ride comfort. In terms of suspension rattle space, IMOPSO shows a clear advantage. IMOPSO reduces the RMS value of suspension rattle space by 10.2%, while

NSGA-II achieves only a 3.3% reduction. This indicates that IMOPSO achieves a better trade-off among performance indicators during the optimization process. While substantially improving comfort and safety, it more effectively controls the suspension rattle space, further reducing the risk of impacting the limit blocks.

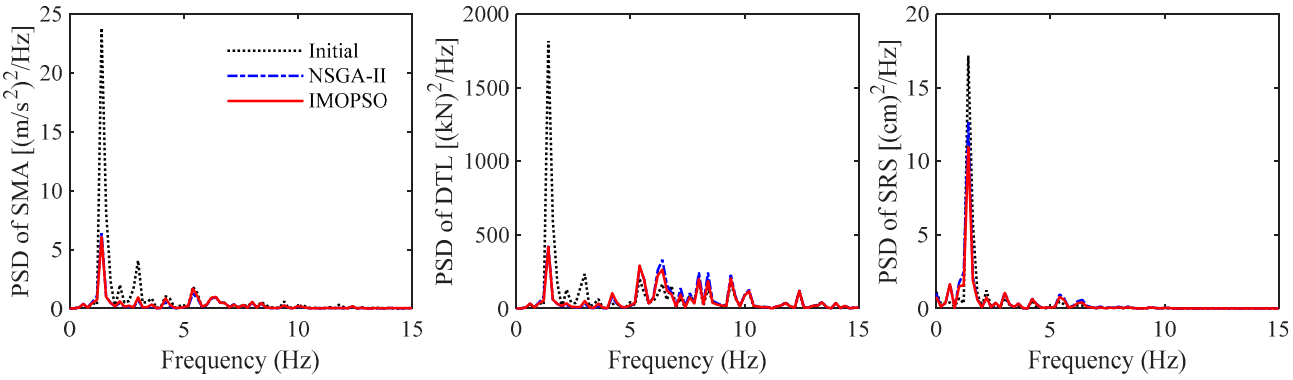

Figure 12. Comparison of vehicle dynamic performance in frequency domain.

Table 5. Comparison of RMS values for vehicle performance indicators on class-C roads.

Vehicle Performance (RMS)	Initial	NSGA-II	IMOPSO
Sprung mass acceleration (m/s^2)	3.496	2.104 (↓ [1] 39.8%)	2.181 (↓ 37.6%)
Dynamic tire load (kN)	36.330	31.715 (↓ 12.7%)	30.584 (↓ 15.8%)
Suspension rattle space (cm)	2.567	2.482 (↓ 3.3%)	2.305 (↓ 10.2%)

[1] ↓ denotes the percentage reduction in vehicle performance metrics after parameter optimization relative to the initial parameters.

To examine the transient impact response characteristics of the hydro-pneumatic suspension, this paper conducts a simulation analysis using bump road excitation as an example, aiming to compare its vibration suppression effect. The mathematical expression of the bump road excitation function adopted in the simulation is as follows:

$$x_r(t) = \begin{cases} \frac{A}{2}\left(1 - \cos\frac{2\pi v t}{l}\right), 0 \le t \le \frac{l}{v} \\ 0, t > \frac{l}{v} \end{cases} \quad (29)$$

where A and l represent the height and length of the bump, respectively. For this study, the parameters are set as $A = 0.1$ m, $l = 5$ m, $v = 25$ km/h.

As shown in Figure 13, under bump road excitation, both optimization schemes significantly reduce the response peaks of sprung mass acceleration and dynamic tire load. It is noteworthy that the suspension rattle space increases during the rebound phase after the wheel leaves the bump, especially for the NSGA-II scheme. This is due to the reduced damping after optimization, which weakens the suppression of the rebound motion. The Pk-Pk comparison data in Table 6 further confirms the excellent performance of the IMOPSO algorithm under transient conditions. On the one hand, IMOPSO achieves the largest reduction in key performance indicators. For the sprung mass acceleration and dynamic tire load under bump road excitation, IMOPSO achieves peak reductions of 38.9% and 44.9%, respectively, which are slightly better than those of NSGA-II (36.0% and 42.3%). This indicates that the IMOPSO scheme can more effectively attenuate vibrations when dealing with severe transient impacts, thereby ensuring ride comfort and wheel grounding performance. On the other hand, IMOPSO achieves a better performance trade-off. Although both algorithms result in an increase in the peak suspension rattle space due to optimization, the increase for IMOPSO (12.4%) is much smaller than that for NSGA-II

(27.6%). This again demonstrates that the IMOPSO algorithm can more intelligently and effectively balance the conflicts between multiple objectives during the optimization search process. It achieves the greatest improvement in key safety and comfort indicators at the cost of a minimal increase in suspension travel.

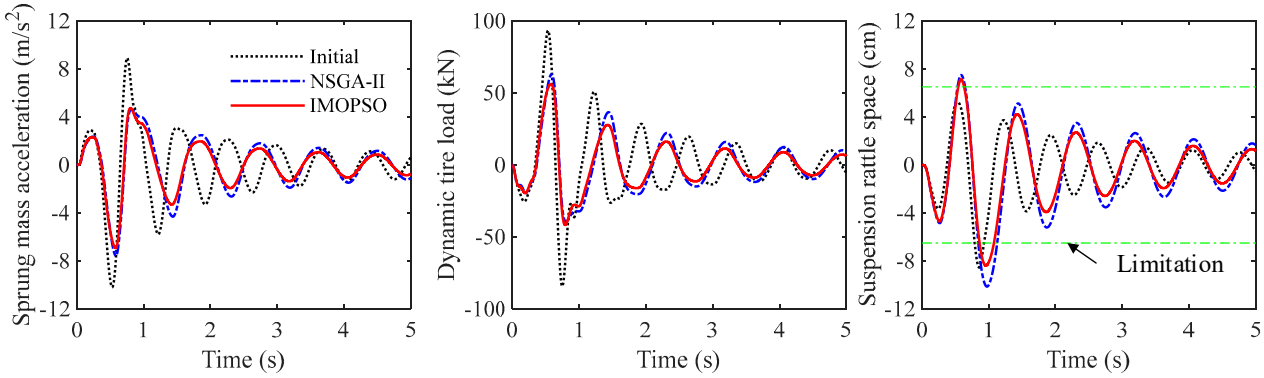

Figure 13. Comparison of vehicle dynamic performance on bump roads.

Table 6. Comparison of Pk-Pk values for vehicle performance indicators on bump roads.

Vehicle Performance (Pk-Pk)	Initial	NSGA-II	IMOPSO
Sprung mass acceleration (m/s^2)	19.079	12.211 (↓ [1] 36.0%)	11.653 (↓ 38.9%)
Dynamic tire load (kN)	177.475	102.342 (↓ 42.3%)	97.786 (↓ 44.9%)
Suspension rattle space (cm)	13.805	17.609 (↑ [2] 27.6%)	15.511 (↑ 12.4%)

[1] ↓ denotes the percentage reduction in vehicle performance metrics after parameter optimization relative to the initial parameters. [2] ↑ donetes the percentage increase in vehicle performance metrics after parameter optimization relative to the initial parameters.

6. Conclusions

This study addresses the multi-objective optimization problem of hydro-pneumatic suspension parameters for mining dump trucks. An accurate gas–liquid coupled dynamic model was established, and a multi-strategy improved multi-objective particle swarm optimization algorithm was proposed. The optimization results demonstrate that under class-C random road excitation, the optimized suspension significantly reduces the RMS values of the sprung mass acceleration and the dynamic tire load by 37.6% and 15.8%, respectively, while also decreasing the suspension rattle space by 10.2%. These improvements systematically enhance ride comfort, wheel grounding performance, and driving safety. Under transient bump road excitation, the Pk-Pk values of the sprung mass acceleration and the dynamic tire load are also reduced by 38.9% and 44.9%, respectively. Although the suspension rattle space increases by 12.4% under this condition, a trade-off analysis indicates that prioritizing ride comfort and wheel grounding performance in transient impact scenarios is more critical, and this performance compromise is deemed reasonable from an engineering perspective. In summary, the optimization method proposed in this study can effectively reconcile the conflicting relationships among multiple performance aspects of hydro-pneumatic suspensions, providing theoretical and methodological support for the refined design of suspension systems in engineering vehicles.

It should be noted that the current study primarily focuses on a deterministic optimization framework under nominal operating conditions. While the proposed method demonstrates significant performance improvements in the considered scenarios, its robustness under probabilistic parameter variations, extreme operational variability, and unmodeled external disturbances has not been systematically evaluated. Furthermore, the validation was conducted using a quarter-vehicle model and two representative road exci-

tations, which may not capture all real-world driving conditions. Future work will extend the present framework to incorporate uncertainty quantification and robust design optimization, consider full-vehicle dynamics and a wider range of operational environments, and validate the approach through physical prototype testing.

Author Contributions: Conceptualization, L.Y. and W.L.; methodology, T.G.; software, M.Z.; validation, M.Z. and G.W.; investigation, G.W.; writing—original draft preparation, T.G.; writing—review and editing, L.Y.; funding acquisition, L.Y. and W.L. All authors have read and agreed to the published version of the manuscript.

Funding: This research was funded by the National Natural Science Foundation Project of China, grant numbers 52504162 and 52502526.

Data Availability Statement: Data are contained within the article.

Conflicts of Interest: The authors declare no conflicts of interest.

Abbreviations

The following abbreviations and variables are used in this manuscript:

Abbreviations	
IMOPSO	Improved Multi-Objective Particle Swarm Optimization
RMS	Root Mean Square
Pk-Pk	Peak-to-Peak
SMA	Sprung Mass Acceleration
SRS	Suspension Rattle Space
DTL	Dynamic Tire Load
Variables	
A	Bump height (m)
A_1	Cross-sectional area of piston (mm^3)
A_2	Effective cross-sectional area of piston rod (mm^3)
A_d	Effective flow areas of check value (mm^3)
A_s	Effective flow areas of damping orifice (mm^3)
C_d	Flow coefficients of check value
C_s	Flow coefficients of damping orifice
c_1	Cognitive coefficient
c_2	Social coefficient
d_0	Damping orifice diameter (mm)
d_1	Piston inner diameter (mm)
d_2	Piston rod outer diameter (mm)
d_{v1}	Equivalent check valve seat hole diameter (mm)
d_{0_min}	Lower bound of d_0 (mm)
d_{0_max}	Upper bound of d_0 (mm)
d_{v1_min}	Lower bound of d_{v1} (mm)
d_{v1_max}	Upper bound of d_{v1} (mm)
d_p	Euclidean distances from the particle to its personal best solution
d_g	Euclidean distances from the particle to global best solution
F	Total suspension output force (kN)
F_c	Suspension damping force (kN)
F_k	Suspension elastic force (kN)
f_0	Lower cut-off frequency (Hz)
f_{cur}	Current particle fitness
f_{avg}	Average particle fitness
f_{diff}	Fitness different
G_q	Road roughness coefficient (m^3)

g	Acceleration due to gravity (m/s^2)
h_0	Initial gas charging height (mm)
h_{0_min}	Lower bound of h_0 (mm)
h_{0_max}	Upper bound of h_0 (mm)
k_t	Tire stiffness (N/m)
l	Bump length (m)
m_s	Sprung mass (kg)
n	Number of damping orifices and check valves
n_0	Reference spatial frequency (m^{-1})
P_0	Initial pressure of gas chamber (Pa)
P_1	Hydraulic pressures in piston chamber (Pa)
P_2	Hydraulic pressures in annular chamber (Pa)
P_b	Instantaneous pressure of gas chamber (Pa)
p_{cur}	Current mutation probability
Q	Total oil exchange flow rate between two chambers (m^3/s)
Q_1	Flow rates through damping orifice (m^3/s)
Q_2	Flow rates through check value (m^3/s)
t_c	Current iteration count
$t_{\max}$	Maximum iteration count
V_0	Initial volume of gas chamber (m^3)
V_b	Instantaneous volume of gas chamber (m^3)
v	Vehicle forward speed (m/s)
x	Suspension relative displacement (m)
$x_{\max}$	Maximum suspension stroke (mm)
$\dot{x}$	Suspension relative speed (m/s)
x_r	Road elevation input (m)
$\dot{x}_r$	Road excitation speed (m/s)
x_u	Vertical displacement of unsprung mass (m)
$\ddot{x}_u$	Vertical acceleration of unsprung mass (m/s^2)
$\ddot{x}_s$	Vertical acceleration of sprung mass (m/s^2)
$\alpha_1, \alpha_2, \beta_1, \beta_2$	Adjustment coefficients
ρ	Density of hydraulic oil (kg/m^3)
γ	Gas polytropic exponent
γ_c	Adjustment factor
ω	Inertia weight
η	Adjustment coefficient for mutation rate
$\omega_{\min}$	Lower bound of ω
$\omega_{\max}$	Upper bound of ω
$w(t)$	Zero-mean white noise
$\sigma_{\ddot{Z}_s}$	RMS value of sprung mass acceleration (m/s^2)
σ_{Fd}	RMS value of dynamic tire load (kN)
Δp	Pressure difference between piston chamber and annular chamber (Pa)
ΔA	Cross-sectional area difference between piston and piston rod (mm^3)
Δx	Suspension rattle space (cm)
δ_ω	Adjustment threshold for ω

References

1. Xie, G.; Ding, R.; Xie, H.; Qin, H.; Bian, Y. Model predictive control-assisted energy management strategy for hybrid mining dump trucks based on speed and slope prediction. *Electronics* **2025**, *14*, 1999. [CrossRef]
2. Wang, S.; Hu, J.; Fang, C.; Yang, B.; Li, D.; Feng, Y.; Xie, Z. Study on load state and service damage mechanism of 100t mining dump truck compartment. *Eng. Fail. Anal.* **2025**, *171*, 109380. [CrossRef]
3. Liu, Q.; Liu, X.; Li, B.; Liu, S.; Li, Y.; Luo, Y.; Sha, T. Characteristics and experimental research on semi-active suspension of mining dump truck under parallel fuzzy control strategy. *Proc. Inst. Mech. Eng. Part C J. Mech. Eng. Sci.* **2025**, *239*, 9174–9190. [CrossRef]

4. Viadero-Monasterio, F.; Boada, B.L.; Zhang, H.; Boada, M.J.L. Integral-based event triggering actuator fault-tolerant control for an active suspension system under a networked communication scheme. *IEEE Trans. Veh. Technol.* **2023**, *72*, 13848–13860.
5. Viadero-Monasterio, F.; Meléndez-Useros, M.; Jiménez-Salas, M.; López Boada, M.J. Avoiding Lyapunov-Krasovskii Functionals: Simple Nonlinear Sampled–Data Control of a Semi-Active Suspension with Magnetorheological Dampers. *Machines* **2025**, *13*, 512. [CrossRef]
6. Parvez, Y.; Chauhan, N.R.; Srivastava, M. Vibration control and comparative analysis of passive and active suspension systems using PID controller with particle swarm optimization. *J. Inst. Eng. (India) Ser. C* **2025**, *106*, 1–19.
7. Tang, H.H.; Ahmad, N.S. Enhanced fuzzy logic control for active suspension systems via hybrid water wave and particle swarm optimization. *Int. J. Control Autom. Syst.* **2025**, *23*, 560–571.
8. Niu, C.; Wang, C.; Jia, Y.; Jia, X.; Gong, B.; Liu, X. Vehicle stability control for active hydro-pneumatic suspension with active disturbance rejection sliding mode control. *J. Vib. Control* **2025**, 10775463251362533. [CrossRef]
9. Lu, R.; Zhang, F.; Cen, S. Automobiles Series Hydro-Pneumatic Spring Active Suspension Structural Design and Nonlinear Control System. *Int. J. Veh. Struct. Syst.* **2024**, *16*, 760–767. [CrossRef]
10. Wu, Y.; Su, D.; Chang, H.; Liu, F.; Wang, W. Research on active disturbance rejection control of hydro-pneumatic suspension of engineering vehicle based on BP neural network. *Proc. Inst. Mech. Eng. Part D J. Automob. Eng.* **2025**, 09544070251340210. [CrossRef]
11. Liu, X.; Wang, G.; Suo, X.; Du, T.; Wang, W.; Zhang, C. Modeling and performance analysis of a hydraulically interconnected suspension for tri-axle mining dump trucks considering pitch-roll resistance. *J. Mech. Sci. Technol.* **2025**, *39*, 483–495.
12. Yang, L.; Wang, R.; Ding, R.; Liu, W.; Zhu, Z. Investigation on the dynamic performance of a new semi-active hydro-pneumatic inerter-based suspension system with MPC control strategy. *Mech. Syst. Signal Process.* **2021**, *154*, 107569.
13. Van Tuan, N.; Chau, N.M.; Minh, N.K. A Study on the nonlinear characteristics of hydro-pneumatic suspension systems for mining dump trucks. *Eng. Technol. Appl. Sci.* **2025**, *15*, 20249–20257. [CrossRef]
14. Li, Z.; Hou, H.; Zhang, Z.; Guo, B.; Song, Y.; Liu, Z. Analysis of vehicle ride comfort and parameter optimization of hydro-pneumatic suspension for heavy duty mining vehicle. *Eng. Lett.* **2024**, *32*, 2145.
15. Chen, Y.; Jiang, M.; Yang, F.; Qian, R.; Zhai, R.; Wang, H.; Xv, S. Research on dynamic modeling and control of magnetorheological hydro-pneumatic suspension. *Actuators* **2025**, *14*, 73. [CrossRef]
16. Jiang, M.; Rui, X.; Wang, G.; Wang, P.; Yang, F.; Zhu, W.; Zhu, H. Modelling and control of magnetorheological hydro-pneumatic suspension system based on multibody system transfer matrix method. *Veh. Syst. Dyn.* **2025**, 1–28. [CrossRef]
17. Wang, G.; Wang, W.; Suo, X.; Du, T.; Wang, D.; Liu, X. Multi-objective parameter optimization of a novel hydraulically interconnected suspension for tri-axle mining dump trucks. *J. Vib. Control* **2025**, *31*, 3585–3598. [CrossRef]
18. Lin, D.; Yang, F.; Li, R.; Zhang, W.; Gong, D. Novel hydro-pneumatic interconnected suspension integrating pipe-connected magnetorheological valve designed based on magnetic gradient pinch mode-experimental study and modelling. *Exp. Tech.* **2025**, *49*, 203–217.
19. Liu, Q.; Liu, X.; Feng, H.; Li, B.; Liu, S.; Luo, Y.; Sha, T. Ride comfort analysis and optimization of a hydro-pneumatic suspension system for a mining dump truck. *Proc. Inst. Mech. Eng. Part D J. Automob. Eng.* **2025**, *239*, 3334–3346.
20. Lin, D.; Yang, F.; Li, R.; Gong, D. Cavitation phenomenon in hydro-pneumatic interconnected suspension: Modeling and parametric analysis. *Nonlinear Dyn.* **2023**, *111*, 8173–8189. [CrossRef]
21. Lv, K.; Wang, J.; Cheng, H.; Wang, H.; Wang, J. Modeling of hydro-pneumatic suspension system with fractional order terms and simulation analysis of road friendliness. *Proc. Inst. Mech. Eng. Part D J. Automob. Eng.* **2023**, *237*, 2605–2615. [CrossRef]
22. Jiang, M.; Rui, X.; Yang, F.; Zhu, W.; Zhu, H.; Han, W. Design and dynamic performance research of MR hydro-pneumatic spring based on multi-physics coupling model. *Nonlinear Dyn.* **2023**, *111*, 8191–8215. [CrossRef]
23. Liu, Y.; Wang, S.; Li, G.; Mao, B.; Dong, Z.; Li, D. Optimal parameter identification of hydro-pneumatic suspension for mine cars. *Int. J. Simul. Multidiscip. Des. Optim.* **2024**, *15*, 26. [CrossRef]
24. Huang, R.; Yin, A.; Shen, Y.; Du, F.; Yang, X. Optimizing hydro-pneumatic inerter suspension for improved ride comfort and handling stability in engineering vehicles using simulated annealing algorithm. *World Electr. Veh. J.* **2024**, *15*, 36. [CrossRef]
25. Yang, L.; Wang, R.; Sun, Z.; Meng, X.; Zhu, Z. Multi-objective optimization design of hydropneumatic suspension with gas-oil emulsion for ride comfort and handling stability of an articulated dumper truck. *Eng. Optim.* **2023**, *55*, 291–310. [CrossRef]
26. Kwon, K.; Seo, M.; Kim, H.; Lee, T.H.; Lee, J.; Min, S. Multi-objective optimisation of hydro-pneumatic suspension with gas-oil emulsion for heavy-duty vehicles. *Veh. Syst. Dyn.* **2020**, *58*, 1146–1165. [CrossRef]
27. Li, Z.; Zhao, S.; Sun, B.; Gao, S.; Gao, Y.; Guo, B.; Liu, Z.; Liu, F. Performance and optimization of the hydropneumatic suspension of high-speed wheeled excavators. *Eng. Lett.* **2023**, *31*, 674.
28. Llopis-Albert, C.; Rubio, F.; Zeng, S. Multiobjective optimization framework for designing a vehicle suspension system. A comparison of optimization algorithms. *Adv. Eng. Softw.* **2023**, *176*, 103375.
29. Fossati, G.G.; Miguel, L.F.F.; Paucar Casas, W.J. Pareto-optimal front for multi-objective optimization of the suspension of a full-vehicle model in the frequency domain. *Eng. Comput.* **2022**, *39*, 916–942. [CrossRef]

30. Liu, W.; Wang, R.; Ding, R.; Meng, X.; Yang, L. On-line estimation of road profile in semi-active suspension based on unsprung mass acceleration. *Mech. Syst. Signal Process.* **2020**, *135*, 106370. [CrossRef]
31. Liu, W.; Wang, R.; Rakheja, S.; Ding, R.; Meng, X.; Sun, D. Vibration analysis and adaptive model predictive control of active suspension for vehicles equipped with non-pneumatic wheels. *J. Vib. Control* **2024**, *30*, 3207–3219. [CrossRef]

Disclaimer/Publisher's Note: The statements, opinions and data contained in all publications are solely those of the individual author(s) and contributor(s) and not of MDPI and/or the editor(s). MDPI and/or the editor(s) disclaim responsibility for any injury to people or property resulting from any ideas, methods, instructions or products referred to in the content.